SPHERIC 2023

Rhodes, Greece, 27-29 June

Proceedings of the 17th International SPHERIC Workshop

Editor
Georgios Fourtakas

SPHERIC 2023

Proceedings of the 17th International SPHERIC Workshop

Rhodes Island, Greece, 27-29 June 2023

Organized by:
School of Engineering
Faculty of Science and Engineering
The University of Manchester
UK

Editor
Georgios Fourtakas

Acknowledgements

Foreword

Dear Delegate,

Since its conception in 2005 with the Inaugural Meeting in Chatou, France, the Smoothed Particle Hydrodynamics rEsearch and Engineering International Community (SPHERIC) has foster, steered and disseminated the development and application of the Smoothed Particle Hydrodynamics (SPH) method in academia and industry alike.

The International SPHERIC Workshops are a unique series of yearly events with exclusive focus on the SPH method and associated particle-based methods. SPH has been widely adopted in the field of computational fluid mechanics, solid mechanics, geomechanics, manufacturing engineering and many other disciplines. The SPH scheme is considered to be the mainstream method for free-surface flows, and multi-phase flows, high non-linear deformation, fracture and fragmentation and, complex physics due to its meshless particle-based nature.

The SPHERIC workshop brings together state-of-the-art developments from academia and novel interdisciplinary applications from industry in a unique blend towards the advancement of the numerical scheme.

It is our pleasure and privilege to host the 17th edition of the International SPHERIC Workshop in Rhodes Island, Greece and I am looking forward to welcoming you for a stimulating and fruitful event.

Sincerely,

Georgios Fourtakas
Chair of the Local Organizing Committee
17th International SPHERIC Workshop

Committees

Scientific Committee

Prof. Renato Vacondio (Università di Parma, Italy)

Prof. Antonio Gil (Swansea University, UK)

Prof. Raj Das (RMIT University, Australia)

Prof. Ben Rogers (University of Manchester, UK)

Dr. Georgios Fourtakas (University of Manchester, UK)

Dr. Chun Hean Lee (Universiy of Glasgow, UK)

Prof Alex Crespo (Universidade de Vigo, Ourense, Spain)

Prof. Abbas Khayyer (Kyoto University, Japan)

Prof. David Le Touzé (Ecole Centrale de Nantes, France)

Dr Nathan Quinlan (National University of Ireland, Galway, Ireland)

Dr. Xiangyu Hu (Technical University of Munich, Germany)

Dr. Pengnan Sun (Sun Yat-sen University, China)

Dr. Tom De Vuyst (University of Hertfordshire, UK)

Dr Christopher Curtis Long (Los Alamos National Laboratory, USA)

Prof. Moncho Gómez-Gesteira (Universidade de Vigo, Spain)

Prof. Xu Fei (Northwestern Polytechnical University, China)

Dr. Rouhollah Fatehi (Persian Gulf University, Iran)

Dr. Nathaniel Albert Trask (Sandia National Laboratories, USA)

Prof. Mehmet Yildiz (Sabanci University, Turkey)

Prof. Andrea Colagrossi (CNR-INM, Italy)

Dr. Matthieu De Leffe (Siemens Digital Industries, France)

Dr. Salvatore Marrone (CNR-INM, Italy)

Prof. Peter Eberhard (University of Stuttgart, Germany)

Dr. Steven Lind (University of Manchester, UK)

Mr. Pierre Sabrowski (Dive Solutions, Germany)

Dr. Giuseppe Bilotta (Istituto Nazionale di Geofisica e Vulcanologia, Italy)

Dr. Ha Bui (Monash University, Australia)

Prof. Stefano Sibilla (Università di Pavia, Italy)

Prof. Antonio Souto Iglesias (UPM, Spain)

Dr Angelo Tafuni (New Jersey Institute of Technology, US)

Local Organising Committee

Dr Georgios Fourtakas

Dr Steven Lind

Dr Abouzied Nasar

Mr Chunze Cen

Mr Ruofeng Feng

Miss Meixuan Lin

Mr Sumanta Laha

Table of contents

Multiple continua and multi-phase flows

Free surface and moving boundaries

Solids and structures

Complex flows I

Geotechnical & disaster applications

Process & manufacturing engineering applications

Complex flows II

A way to increase the convergence-order in SPH

Julien Michel[(a),(b)], Andrea Colagrossi[(a),(b)], David Le Touzé[(b)], Matteo Antuono[(a)], Salvatore Marrone[(a)]

(a) CNR-INM Institute of marine engineering, National Research Council, Rome, Italy
(b) Ecole Centrale Nantes, LHEEA research dept. (ECN and CNRS), Nantes, France
julien.michel@inm.cnr.it

Abstract—Smoothed Particle Hydrodynamics (SPH) schemes generally result from a compromise between the need for conservation of the main global quantities (global mass, linear and angular momenta) and consistency of the SPH mollified operators towards the exact ones. In the present work, a globally non-conservative but locally accurate pressure gradient approximation is adopted, resulting in a novel high-order weakly-compressible SPH scheme, which also prevents Tensile Instability occurrences. To fulfill the dynamic free-surface boundary condition, a switch between the non-conservative and conservative formulations is retained, the latter being preferred in a thin region close to the free-surface. Regular particle distributions are maintained thanks to recent improvements in Particle Shifting Techniques. The latter are taken into account within the continuity and momentum equations through a quasi-Lagrangian formalism. The numerical diffusion is obtained using Riemann solvers, with a reconstruction/limitation of the left and right states based on the Monotonic Upstream-centered Scheme for Conservation Laws (MUSCL) technique, allowing for low numerical dissipation without tuning parameters. The numerical investigation is carried out on several problems characterized by different flow features and showing the advantages of the present scheme with respect to conservative formulations. Since the proposed formulation does not intrinsically guarantee momenta conservation, the latter are monitored proving that the overall errors are generally acceptable.

I. INTRODUCTION

SPH is a particle method based on the discretization of the computational domain in particles without topological connections. In this framework a differential operator at a certain position is represented through a convolution summation among neighbouring particles via a chosen weight function, also known as kernel function. The representation of the differential operators is not unique and several properties of SPH both globally (*i.e.* global conservation properties) and locally (accuracy and consistency of the operators) depend on the specific formulation. In general, this is a compromise between the need for conservation of the main global quantities (*i.e.* global mass, linear and angular momenta) and consistency of the SPH mollified operators towards the exact ones.

The first application of the SPH method to free-surface flows considering the fluid as a weakly-compressible medium was derived in a conservative formalism (see *e.g.* [16]) that is, through the use of differential operators ensuring exact mass and momenta conservation. A remarkable property was the intrinsic fulfillment of the dynamic free-surface boundary condition [4]. On the other hand, the accuracy of such formulation was rather low (between the first and second order) and was very sensitive to particle disorder, which

rapidly deteriorates the convergence of the scheme [20]. Additionally, the conservative formulations are prone to the onset of Tensile Instability (TI), an unwanted phenomenon that introduces noise in the fluid flow solution and, in the worst case, generation of voids inside the regions characterized by large negative pressure. To improve the accuracy of such formulations, maintaining regular particle distribution was a key point, and substantial improvements have been achieved through the implementation of Particle Shifting Techniques (PSTs) (see, *e.g.*, [11], [18]). Concomitantly, PSTs were taken into account within the continuity and momentum equations through quasi-Lagrangian formalism, as in [18].

On the other hand, non-conservative formulations were proposed to overcome some drawbacks of the conservative schemes and increase the interpolation accuracy of the SPH method. It was firstly achieved by Randles & Libersky [21] in the solid mechanics context, thanks to the introduction of renormalized operators allowing for the exact gradient approximation of a linear field. Then, again in the solid mechanics field, Dilts [7] proposed a Moving Least Square (MLS) method to approximate the SPH operators and consequently suppress Tensile Instability occurrences. Such renormalized operators were then adapted to weakly-compressible free-surface flows by Oger *et al.* [17]: since the dynamic free-surface boundary condition is not ensured with non-conservative formulations [4], a switch between conservative and non-conservative formulations was performed depending on the particle position with respect to the free-surface. Because PSTs were not yet developed, the study was limited to the pure Lagrangian framework. The MLS method was also adapted to the weakly-compressible field by Le Touzé *et al.* [9] where the pressure condition was imposed explicitly at the free-surface.

More recently, a switch between conservative and non-conservative formulations was adopted by Sun *et al.* [22], [23] to counteract Tensile Instability in case of strong negative pressure, *e.g.* in vortex cores. The switch depended this time on the pressure sign: non-conservative formulation was preferred in case of negative pressure whereas the conservative formulation was used in zones of positive pressure; the latter was also maintained close to the free-surface.

In the present work, a non-conservative formulation presenting similarities with the one of Oger *et al.* [17] is investigated. The pressure gradient is approximated as in [17], *i.e.* considering the non-conservative formulation far from the free-surface (and, therefore, free from Tensile Instability) and the conservative one close to the free-surface. A renormalized operator

is retained, ensuring exact reproduction of the gradient of a linear pressure field. Regular particle distribution and therefore accurate interpolation of the SPH operators are maintained thanks to PST, filling the gap with the works by [9], [17]. This PST is taken into account within the constitutive equations considering the quasi-Lagrangian formalism firstly derived by Sun *et al.* [22] and then adapted to Riemann solver in [14]. Since the present paper aims at a low-dissipation scheme, Riemann solver are retained, filling another gap with the works by [9], [17]. The proposed formulation does not ensuring momenta conservation, a specific attention is paid on this aspect and the momenta are monitored during the simulations. The investigation is performed for various configurations on dedicated test cases.

II. DERIVATION OF THE SCHEME

In this section the proposed formulation is presented, the five key points being: (i) use of PST to obtain regular particle distributions and then accurate interpolation of the SPH operators; (ii) use of quasi-Lagrangian derivative $d(\bullet)/dt = D(\bullet)/dt + \nabla(\bullet) \cdot \delta u$ to take into account the PST in the constitutive equation (δu being the PST velocity and $D(\bullet)/dt$ the Lagrangian derivative); (iii) use of a renormalized pressure gradient inside the fluid to avoid Tensile Instability and then increase the accuracy order of this operator; (iv) use of a conservative pressure gradient operator in the free-surface region to ensure free-surface dynamic boundary condition; (v) use of diffusive terms obtained by means of Riemann solver. With these choices the scheme reads:

$$\frac{d\rho_i}{dt} = -\rho_i \mathrm{div}(\boldsymbol{u}_i) - \rho_i \mathrm{div}(\boldsymbol{\delta u}_i) + \mathrm{div}(\rho_i \boldsymbol{\delta u}_i) + \Theta^\rho_{i,Rie}$$

$$m_i \frac{d\boldsymbol{u}_i}{dt} = -V_i \boldsymbol{\nabla} P_i + m_i \boldsymbol{f_i} + V_i \mathrm{div}(\rho_i \boldsymbol{u}_i \otimes \boldsymbol{\delta u}_i) + \boldsymbol{\Theta}^{\boldsymbol{u}}_{i,Rie}$$

$$\frac{d\boldsymbol{x}_i}{dt} = \boldsymbol{u}_i + \boldsymbol{\delta u}_i, \quad V_i(t) = m_i / \rho_i(t), \quad P_i = c_0^2(\rho_i - \rho_0), \tag{1}$$

where the subscript i refers to the particle i. ρ_i and V_i are the density and volume respectively, and the mass m_i is supposed constant in time and set using the initial volume and density values as $m_i = \rho_i(0)V_i(0)$. $\boldsymbol{x}_i$ is the material point position, $\boldsymbol{u}_i$ the fluid velocity, $\boldsymbol{f}_i$ the external volume forces, P_i the pressure, ρ_0 and c_0 the nominal density and speed of sound respectively. Since the weakly-compressible assumption is used, the latter is chosen as:

$$c_0 \geq 10 \max\left(U_{max}, \sqrt{(\Delta p)_{max}/\rho} \right)$$

where U_{max} and $(\Delta p)_{max}$ stand respectively for the expected maximum velocity and pressure variation within the fluid domain. The continuity equation and the term due to PST within the momentum equation are identical to [14] and the corresponding terms are:

$$\rho_i \mathrm{div}(\boldsymbol{u}_i) = \rho_i \sum_j (\boldsymbol{u}_j - \boldsymbol{u}_i) \cdot \boldsymbol{\nabla}_i W_{ij} V_j$$

$$\rho_i \mathrm{div}(\boldsymbol{\delta u}_i) = \rho_i \sum_j (\boldsymbol{\delta u}_j - \boldsymbol{\delta u}_i) \cdot \boldsymbol{\nabla}_i W_{ij} V_j$$

$$\mathrm{div}(\rho_i \boldsymbol{\delta u}_i) = \sum_j (\rho_i \boldsymbol{\delta u}_i + \rho_j \boldsymbol{\delta u}_j) \cdot \boldsymbol{\nabla}_i W_{ij} V_j$$

$$\Theta^\rho_{i,Rie} = -\rho_i \sum_j (2\boldsymbol{u_E} - (\boldsymbol{u}_i + \boldsymbol{u}_j)) \cdot \boldsymbol{\nabla}_i W_{ij} V_j$$

$$V_i \mathrm{div}(\rho_i \boldsymbol{u}_i \otimes \boldsymbol{\delta u}_i) = \sum_j (\rho_i \boldsymbol{u}_i \otimes \boldsymbol{\delta u}_i + \rho_j \boldsymbol{u}_j \otimes \boldsymbol{\delta u}_j) \boldsymbol{\nabla}_i W_{ij} V_j V_i$$

where W is the kernel function (hereinafter a $\mathcal{C}^2$-Wendland kernel is adopted), the subscript j indicates the neighbour particles to the i-th particle and $\boldsymbol{u}_E$ is the velocity solution of the Riemann problem (see [14] for details).
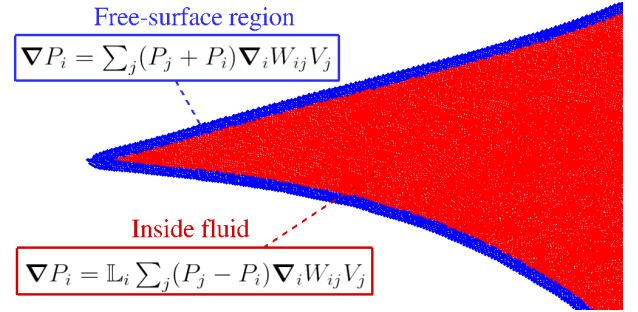
Fig. 1. Definition of free-surface region and inner particles along with the related pressure gradient approximations: the free-surface region is defined as the union of free-surface particles and particles having at least a free-surface particle within their kernel support; inner particles are particles that do not interact with free-surface particles. $\mathbb{L}_i$ is the renormalization matrix defined in Eq. (3).

Differently from [14], the pressure gradient is here approximated by following [17], *i.e.* considering a switch between the non-conservative and conservative formulations, depending on the particle position with respect to the free-surface: the former is used inside the fluid domain, while the latter is adopted in a thin region close to the free-surface. Precisely, the algorithm derived in [13] is used to detect particles located at the free-surface. The free-surface region is then defined as the union of these free-surface particles with particles having at least one free-surface particle within their kernel support. For particles within this free-surface region the conservative formulation is used, this choice being motivated by the need of fulfilling the dynamic free-surface boundary condition (see [4] for details). By contrast, for inner fluid particles noted hereinafter $\mathcal{I}$ and corresponding to particles without free-surface particle within their kernel support, the non-conservative formulation is retained, as represented in Fig. 1. Incidentally, a second condition for the application of the non-conservative formulation (namely, $\Gamma_i \geq 0.95$ where $\Gamma_i = \sum_j W_{ij} V_j$) is necessary to avoid that the presence of a small gap between different fluid portions leads some particles to be regarded as inner particles. Finally, the pressure gradient approximation reads:

$$\boldsymbol{\nabla} P_i = \begin{cases} \mathbb{L}_i \sum_j (P_j - P_i) \boldsymbol{\nabla}_i W_{ij} V_j & \text{if } i \in \mathcal{I} \, \& \, \Gamma_i \geq 0.95 \\ \sum_j (P_j + P_i) \boldsymbol{\nabla}_i W_{ij} V_j & \text{otherwise} \end{cases} \quad (2)$$

where $\mathbb{L}_i$ is the renormalization matrix [21] ensuring the exact gradient approximation of a linear pressure field:

$$\mathbb{L}_i = \left[\sum_j (\boldsymbol{x}_j - \boldsymbol{x}_i) \otimes \boldsymbol{\nabla}_i W_{ij} V_j \right]^{-1} \quad (3)$$

In [14], the diffusive term due to Riemann solvers in the momentum equation was expressed following the idea of [19], *i.e.* by substituting the arithmetic mean $(P_j + P_i)/2$ by the Riemann problem solution P_E within the pressure gradient approximation as:

$$\begin{aligned} \sum_j (P_j + P_i) \boldsymbol{\nabla}_i W_{ij} V_j &= \sum_j 2 \frac{P_j + P_i}{2} \boldsymbol{\nabla}_i W_{ij} V_j \\ &\approx \sum_j 2 P_E \boldsymbol{\nabla}_i W_{ij} V_j \, . \end{aligned} \quad (4)$$

In the present work the proceed of [14] is re-used, but considering the pressure gradient approximation (2): the first line of (2) is then rewritten as $\mathbb{L}_i \sum_j (P_j - P_i) \boldsymbol{\nabla}_i W_{ij} V_j = \mathbb{L}_i \sum_j 2 \left[(P_j + P_i)/2 - P_i \right] \boldsymbol{\nabla}_i W_{ij} V_j$ where the term $(P_j + P_i)/2$ is substituted by P_E; for the second line of (2) the expression (4) is retained as it is. Thus, noting $\Theta_{ij} = 2 P_E - (P_i + P_j)$, the diffusive term within the momentum equation due to Riemann solver reads:

$$\boldsymbol{\Theta}_{i,Rie}^{\boldsymbol{u}} = \begin{cases} -\mathbb{L}_i \sum_j \Theta_{ij} \boldsymbol{\nabla}_i W_{ij} V_j V_i & \text{if } i \in \mathcal{I} \, \& \, \Gamma_i > 0.95 \\ -\sum_j \Theta_{ij} \boldsymbol{\nabla}_i W_{ij} V_j V_i & \text{otherwise} \end{cases} \quad (5)$$

Finally, the scheme is integrated in time by using a 4th-order Runge-Kutta scheme, with the following Courant-Friedrichs-Lewy number:

$$\Delta t = CFL_h \frac{R_w}{c_0} \quad ; \quad CFL_h = 0.5 \quad (6)$$

A ratio $R_w/\Delta x = 4$ is used in all the numerical simulations, where R_w is the radius of the kernel support and Δx is the initial particle distance.

Before proceeding to the next Section, we just highlight some important points. Within the free-surface region (or when $\Gamma_i < 0.95$), the scheme in the system (1) is equivalent to the *QL-MassCons* scheme derived in [14]. For inner particles characterized by $\Gamma_i \geq 0.95$ the difference resides in the pressure gradient approximation. The mass is intrinsically conserved but linear and angular momentum are not. However, the proposed formulation is invariant by change of pressure reference (for internal flows) and free from the Tensile Instability.

III. PARTICLE SHIFTING TECHNIQUE (PST)

The PST derived in [15] is used with the additional condition proposed in [14] to limit density variations induced by PST within quasi-Lagrangian SPH formulations. Following [8], the shifting is performed tangentially to the free-surface in all the free-surface region. The first step of the PST consists in computing a non-dimensional vector pointing towards zones with low concentration of particles $\boldsymbol{J}_i$ as:

$$\boldsymbol{J}_i = -R_i \, (R_i/\Delta x)^3 \sum_j \left[1 + 0.2 \left(\frac{W_{ij}}{W(\Delta x)} \right)^4 \right] \boldsymbol{\nabla}_i W_{ij}^* V_j \quad (7)$$

where $R_i = \min \left(R_w, \max \left(\Delta x, d_i^{FS} \right) \right)$, d_i^{FS} is the distance between particle i and its closest free-surface particle, and W^* is the kernel function with support radius R_i. In the free-surface region, *i.e.* for $i \notin \mathcal{I}$, to ensure that the kinematic free-surface condition is fulfilled, $\boldsymbol{J}_i$ is projected in the direction tangential to the free-surface. The projected vector reads:

$$\boldsymbol{J}_i^{\perp} = \boldsymbol{J}_i - (\boldsymbol{J}_i \cdot \tilde{\boldsymbol{n}}_i) \, \tilde{\boldsymbol{n}}_i \quad (8)$$

where $\tilde{\boldsymbol{n}}_i$ is the normal vector in the free-surface region computed as in [15]. For particles inside fluid $\tilde{\boldsymbol{n}}_i = \boldsymbol{0}$. Finally, the PST velocity $\boldsymbol{\delta u}_i$ is computed as follows:

$$\boldsymbol{\delta u}_i = \boldsymbol{J}_i^{\perp} \min \left(U_i^{char} \, ; \, \frac{1}{2} \frac{R_w}{\Delta x} \frac{U_i^{char}}{\|\boldsymbol{J}_i^{\perp}\|} \, ; \, \frac{\epsilon}{2 \Delta t |\boldsymbol{J}_i^{\perp} \cdot \boldsymbol{\nabla} \Gamma_i|} \right) \quad (9)$$

where $U_i^{char} = 0.5 \max_j \left(\left| (\boldsymbol{u}_j - \boldsymbol{u}_i) \cdot \frac{(\boldsymbol{x}_j - \boldsymbol{x}_i)}{\|\boldsymbol{x}_j - \boldsymbol{x}_i\|} \right| \right)$ is the characteristic velocity used in [15] to ensure that $\boldsymbol{\delta u}_i$ is $\mathcal{O}(\Delta x)$. The third limitation ensures that the shifting velocity induces small density variations [14]. Precisely, ϵ is the maximum density variation allowed within one time-step Δt. In all the simulations $\epsilon = 5.0 \times 10^{-5}$. Finally, $\boldsymbol{\nabla} \Gamma_i = \sum_j \boldsymbol{\nabla}_i W_{ij} V_j$.

IV. NUMERICAL RESULTS

The present section is dedicated to the discussion of the numerical results. Four benchmarks are chosen to carry out the discussion, all in two dimensions. A comparison with analytical solution is provided when applicable. In order to discuss the benefits and drawbacks of using a non-conservative pressure gradient, the *QL-MassCons* scheme derived in [14] is used all along the discussion as a comparison baseline. As the only difference between the two formulations is specifically the pressure gradient approximation, it allows for comparing conservative and non-conservative formulation while keeping the other components of the scheme unchanged.

A. Case of an inviscid internal flow: Taylor-Green vortices

The first test case under investigation is the Taylor-Green vortices. Since an inviscid fluid is considered, it allows for measuring the numerical dissipation for an internal flow. The analytical solution in terms of velocity and pressure is given by:
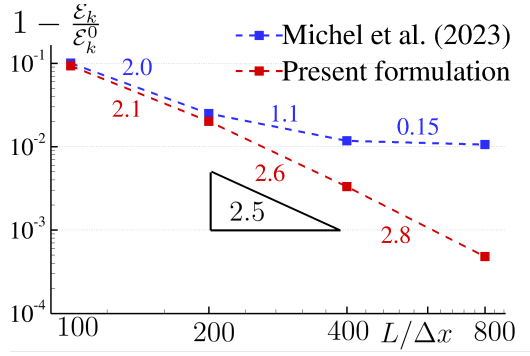
Fig. 2. Inviscid Taylor-Green vortices. Energy dissipated at $tU/L = 5$ for four spatial resolutions with the present formulation, compared to *QL-MassCons* scheme of [14]; the order rate between two spatial resolutions are indicated with corresponding colors
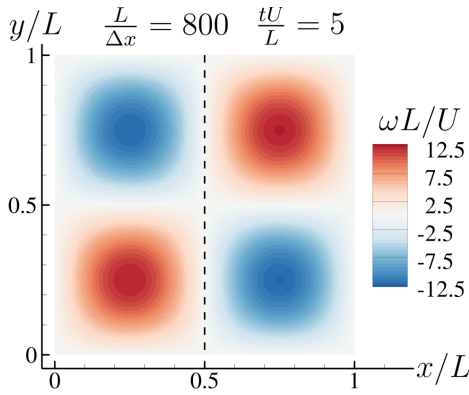

Fig. 3. Inviscid Taylor-Green vortices. Vorticity field obtained with the proposed formulation at $tU/L = 5$ for $L/\Delta x = 800$. The analytical solution is represented in the right part on the black dashed-line (*i.e.* for $x/L > 0.5$).

$$\begin{cases} u_x &= U \sin\left(2\pi x/L\right)\cos\left(2\pi y/L\right) \\ u_y &= -U \cos\left(2\pi x/L\right)\sin\left(2\pi y/L\right) \\ p &= \frac{\rho_0 U^2}{2}\frac{1}{2}\left[\cos\left(4\pi x/L\right) + \cos\left(4\pi y/L\right)\right] \end{cases} \tag{10}$$

in a periodic domain of size $[0, L] \times [0, L]$. The reference scales are the length L, the velocity U, the time L/U, the pressure $\rho_0 U^2/2$, and the initial kinetic energy $\mathcal{E}_k^0$. The speed of sound is chosen as $c_0 = 10U$ and the study is carried out for 4 spatial resolutions ranging from $L/\Delta x = 100$ to $L/\Delta x = 800$, until time $tU/L \leq 5$. As shown in Fig. 2 the present formulation allows for maintaining a convergence-order rate between the 2nd and 3rd order until $L/\Delta x = 800$, while an inevitable saturation is observed with the *QL-MassCons* scheme (see [14] for details).

In Fig. 3 the vorticity field obtained with the proposed formulation with the spatial resolution $L/\Delta x = 800$ is represented at $tU/L = 5$. The analytical solution is reported for $x/L > 0.5$ for qualitative comparison purposes. As observed the results are in good accordance with the analytic solution, the only mismatch being located at the center of vortices where the vorticity picks are smoothed with respect to the analytic solution.

B. Case of an inviscid flow without free-surface deformation: inviscid rotating circular fluid domain with non-uniform angular velocity

(a) Vorticity field, QL-MassCons scheme [14]

(b) Vorticity field, present formulation
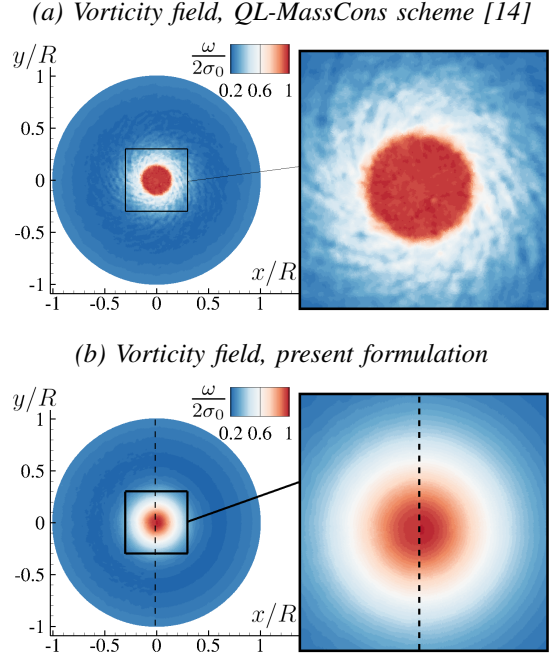
Fig. 4. Inviscid rotating circular fluid domain with $B/\sigma_0 = \pi/12$. Vorticity field obtained with $R/\Delta x = 400$ at $t\sigma_0 = 100$ with the *QL-MassCons* scheme derived in [14] (top) and with the present formulation (bottom). In the bottom part, the analytical solution is provided in the right part of the black dashed line (*i.e.* for $x/R > 0$) for qualitative comparison purposes.

The second test case under investigation consists in a rotating circular patch of fluid of radius R with a non-uniform angular velocity distribution [5]. It constitutes an interesting benchmark to measure the numerical dissipation of the scheme when no free-surface deformations occur. The analytical solution in polar coordinates reads:

$$\begin{cases} u_\theta(r) &= r\,\sigma(r)\,; \quad u_r(r) = 0 \\ p(r) &= -\rho_0 \int_r^R s\,\sigma(s)^2 + \rho_0\,\frac{B^2}{2}\left(R^2 - r^2\right) \end{cases} \tag{11}$$

where $\sigma(r) = \sigma_0\left[\frac{\ell^2}{\ell^2 + r^2} + \frac{2R\ell^2}{(\ell^2 + R^2)^2}\,r\right]$ is the non-uniform angular velocity, ℓ is a shape parameter set as $\ell^2 = 0.1\,R^2$ as in [5]. σ_0 and B are dimensional parameters of frequency dimension standing respectively for the angular velocity amplitude at the center of fluid domain and the centripetal volume force $\boldsymbol{f} = -B^2 r\boldsymbol{e_r}$. In the present work B is set as $B/\sigma_0 = \pi/12$ to obtain negative pressure in most of the fluid domain without adverse pressure gradient at the free-surface. The reference variables are the length R, the time $1/\sigma_0$, the velocity $R\sigma_0$, the pressure $\rho_0 R^2\sigma_0^2$, the maximum vorticity $2\sigma_0$ and the mechanical energy $\mathcal{E}_m^0$. The speed of sound is chosen as $c_0 = 2.7R\sigma_0$ and the study is performed for four spatial resolution going from $R/\Delta x = 50$ to $R/\Delta x = 400$ and for $t\sigma_0 \leq 100$.
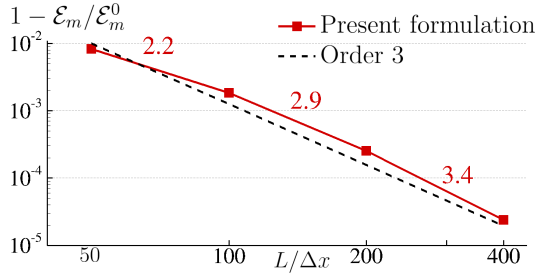
Fig. 5. Inviscid rotating circular fluid domain with $B/\sigma_0 = \pi/12$. Mechanical energy obtained at $t\sigma_0 = 100$, as a function of the spatial resolution.
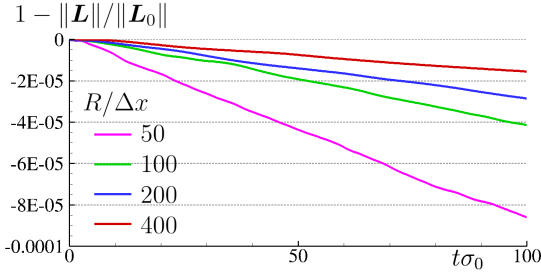

Fig. 6. Inviscid rotating circular fluid domain with $B/\sigma_0 = \pi/12$. Temporal evolution of the angular momentum obtained with the present formulation for four spatial resolutions.

Since the pressure is negative in most of the fluid domain, Tensile Instability is expected to occur with a conservative pressure gradient formulation, introducing disorder in the particles distribution. The PST acts against the Tensile Instability preventing unphysical cavities in the fluid domain, but noise in the fluid flow solution remains (top plot of Fig. 4). By contrast, the present formulation is by nature free from Tensile Instability and the vorticity field obtained with the proposed formulation is in good agreement with respect to the analytical solution, plotted for $x/R > 0$ (see bottom plot of Fig. 4)). In Fig. 5 the energy dissipated at $t\sigma_0 = 100$ as a function of the spatial resolution is plotted and a 3rd-order of convergence is observed in this test case. Finally, the temporal evolution of the angular momentum is given in Fig. 6. At $t\sigma_0 = 100$ the maximum error observed with the coarsest resolution is about 1×10^{-4} of the initial angular momentum. Furthermore, it converges towards 0 with an order of about 0.5.

C. Case of an inviscid periodic flow in long-time simulation with small free-surface deformation: standing wave

The fourth test case under investigation consists in the evolution of an inviscid standing wave over finite depth, often used in SPH to study the numerical dissipation of different schemes (see, *e.g.*, [1], [10]). The fluid height is fixed to $H = L/2$ and $k = 2\pi/\lambda$ is the wave number with $\lambda = L$ the wave length. The crest to trough amplitude is fixed to $0.2\,H$ as represented in Fig. 7. Noting g the gravity acceleration amplitude, initial pressure and velocity are set like in [1] as:
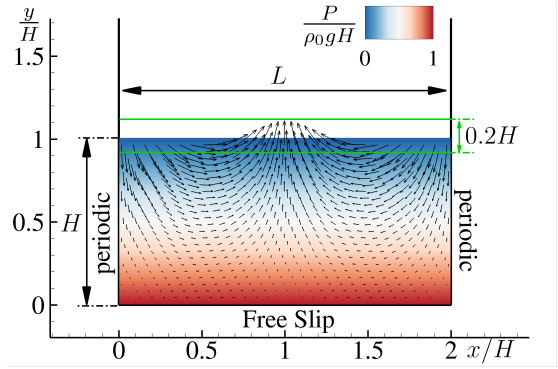
Fig. 7. Inviscid standing wave. Description of the test case and initial conditions.
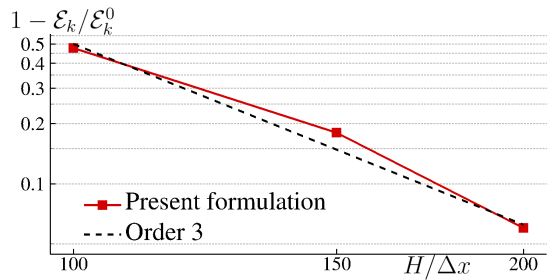
Fig. 8. Inviscid standing wave. Convergence order measured on the envelop at $t/T \approx 100$; the $3^{rd}-$ order convergence rate is also indicated.

$$\begin{cases} u_x^0 = U\cosh(ky)\sin(kx) \\ u_y^0 = -U\sinh(ky)\cos(kx) \\ p^0 = \rho_0 g(H-y) \end{cases} ; \quad U = \frac{0.2\,H\sqrt{gk}}{2\sqrt{\tanh(kH)}\cosh(kH)}$$

Due to the amplitude of the standing wave, the linear potential theory is not sufficient to capture the physics and the $3^{rd}-$order solution of [3] is used as a reference solution. The reference variables are the length H, the pressure $\rho_0 gH$, the oscillation period T and the initial kinetic energy $\mathcal{E}_k^0$. The speed of sound is chosen as $c_0 = 10\sqrt{gH}$. The free-slip boundary condition considered in the bottom part of the tank (see Fig. 7) is modelled using the classical ghost particle method [6] and the PST velocity δu_i is mirrored in the normal direction of the boundary, as proposed in [18].

First, as shown in Fig. 8, a 3rd-order of accuracy is recovered concerning the kinetic energy, with a relative error of about 5% during the last oscillation period for the finest spatial resolution. In Fig. 9 the temporal evolution of the free-surface elevation η at the center of the fluid domain $x/H = 1$ is plotted for three spatial resolutions; the last five oscillation periods are shown and the $3^{rd}-$ order analytical solution of [3] is also plotted. The pick amplitude converges towards the reference solution as the spatial resolution increases, and the relative error during the last oscillation with $H/\Delta x = 200$ are about 4% and 6% respectively for the crest and trough elevation. The frequency also converges towards the reference solution and, with the finest spatial resolution an error of

Fig. 9. Inviscid standing wave. Temporal evolution of the free-surface elevation η at the center of the fluid domain (*i.e.* $x/H = 1$) for three spatial resolutions, along with the 3rd−order analytical solution of [3]; only the last 5 oscillation periods are represented.
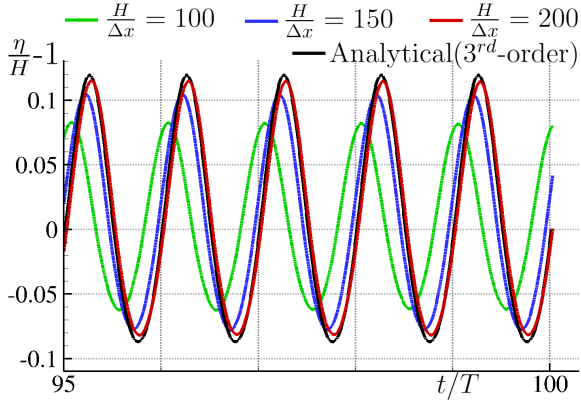
0.01% per oscillation is observed. This good accordance with the reference solution is confirmed in Fig. 10 where the pressure field obtained in the last oscillation for $H/\Delta x = 200$ is plotted, in addition to the analytical free-surface [3].
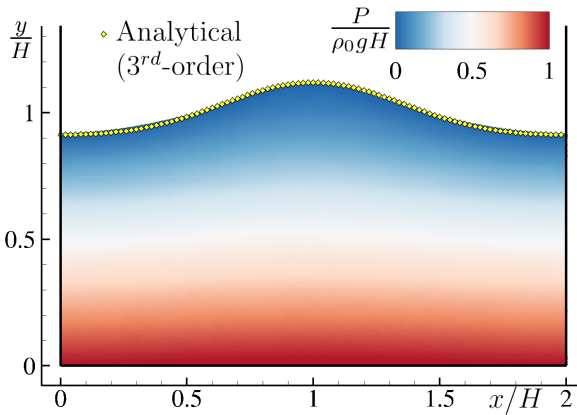

Fig. 10. Inviscid standing wave. Snapshots of the flow field during the last oscillation period at $t = 99.25\,T$ obtained with $H/\Delta x = 200$. The free surface of the 3rd−order analytical solution [3] is plotted for qualitative comparison.
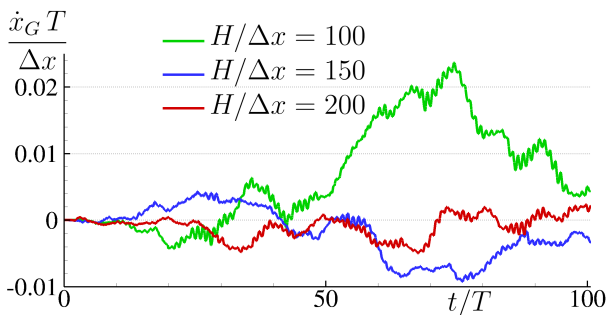

Fig. 11. Inviscid standing wave. Temporal evolution of the x-component of velocity of the fluid center of gravity for three spatial resolutions. Δx is the particle spacing corresponding to the related spatial resolution and, therefore, diminishes as the spatial resolution increases.

Finally, to check the linear momentum conservation, the temporal evolution of the horizontal component of the velocity of the center of gravity $\dot{x}_G$ is plotted in Fig. 11. The quantity $\dot{x}_G T$ represents the horizontal displacement of the center of gravity during one period, and this quantity is compared to the initial particle spacing Δx (which furthermore diminishes as the spatial resolution increases). For the coarsest spatial resolution, the maximum displacement during one period is in any case less than $2.5\%\,\Delta x$. Moreover, this error diminishes as the spatial resolution increases and reaches $0.5\%\,\Delta x$ for $H/\Delta x = 200$.

D. Case of an inviscid fluid with spatial and temporal discontinuities: fluid impact
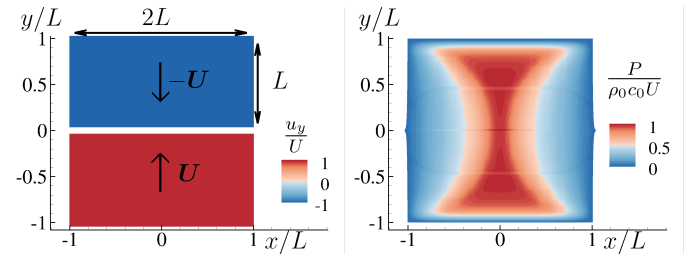

Fig. 12. Impact of two identical inviscid fluid patches. Left: initial velocity field. Right: pressure field obtained with $L/\Delta x = 400$ at $tU/L = 0.048$.

The last test case under investigation consists in the impact in the normal direction of two identical rectangular inviscid fluid patches of size $[2L, L]$. The two patches impact each other with velocities $\boldsymbol{U}$ and $-\boldsymbol{U}$ respectively, as represented in the left plot of Fig. 12. The reference scales are the length L, the velocity U, the time L/U, the pressure $\rho_0 c_0 U$ and the initial kinetic energy $\mathcal{E}_k^0 = 2\rho_0 L^2 U^2$, where the notation $U = \|\boldsymbol{U}\|$ is used hereinafter. The particles are initialized on a Cartesian lattice with initial pressure and velocity $P = 0$, $u_x = 0$ and $u_y = \pm U$. The speed of sound is chosen as $c_0 = 100U$ like in [12], [14] in order to limit the density variation to about 1%. As in [14], a small gap of length $0.08L$ between the two fluid patches is considered in the initial configuration (see left plot of Fig. 12), in order to represent impact appearing in more complex cases. After the contact of the two fluid surfaces (see right plot of Fig. 12), an acoustic wave front propagates in the vertical direction from the contact line towards the free surface with intensity of order $\rho_0 c_0 U$; simultaneously, a rarefaction wave propagates from the lateral free surfaces towards the center. Finally, an horizontal elongation is experienced by the two joint fluid patches, with acoustic waves reflection on the free-surface as the fluid patch elongates. Initially formulated in [24] for an incompressible fluid, this problem was then studied for validation of weakly-compressible SPH models (see, *e.g.*, [12], [14]). In the latter case, the total energy $\mathcal{E}_k + \mathcal{E}_c$ is theoretically conserved, with a periodic energy transfer from kinetic to compressible energy (and viceversa) occurring at each acoustic wave reflection.

For the present work, the main interest of this benchmark resides on the temporal and spatial discontinuity which characterizes the collision of the two patches. When the patches impact each other, the particles in the impact area are, indeed, suddenly detected as inside fluid particles. Consequently, an abrupt change on the pressure gradient formulation occurs as it goes from its conservative to its non-conservative formulation.

In the top part of Fig. 13, the temporal evolution of the total energy obtained for four spatial resolutions is represented. The main part of the energy dissipation occurs during the impact stage, *i.e.* for $tU/L < 0.04$. After that instant, the periodic transfer between kinetic and compressible energies is maintained (see bottom part of Fig. 13), and for spatial resolutions $L/\Delta x \geq 200$ this energy transfer occurs with negligible numerical dissipation. This behavior is different to what observed in [14] with a conservative pressure gradient formulation, where additional dissipation was observed due to the strong negative pressure appearing periodically in the fluid domain and implying Tensile Instability occurrences. A 1st−order convergence is observed from $L/\Delta x \geq 100$ but this lower accuracy-order (with respect to the previous test cases) is coherent with the presence of a discontinuity.
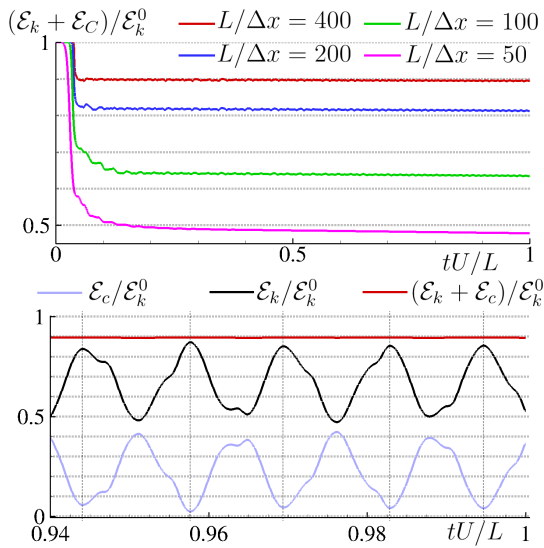

Fig. 13.   Impact of two identical inviscid fluid patches. Top: temporal evolution of the total energy for four spatial resolutions. Bottom: temporal evolution of the kinetic, compressible and total energies for $L/\Delta x = 400$ for the last portion of the simulation time history.

Regarding the kinematics, in the top plot of Fig. 14 the results are compared to those obtained in [12] with an incompressible Finite Volume method (LS-FVM) at $tU/L = 0.207$ and a good agreement is found. Since no reference solution is available in the literature after this instant, the free-surface shape is compared in the bottom plot to the one obtained with the *QL-MassCons* scheme of [14], showing again a good agreement. Finally, in order to check the linear momentum conservation, the vertical component of the velocity of the center of gravity $\dot{y}_G$ is plotted in Fig. 15, normalized by the
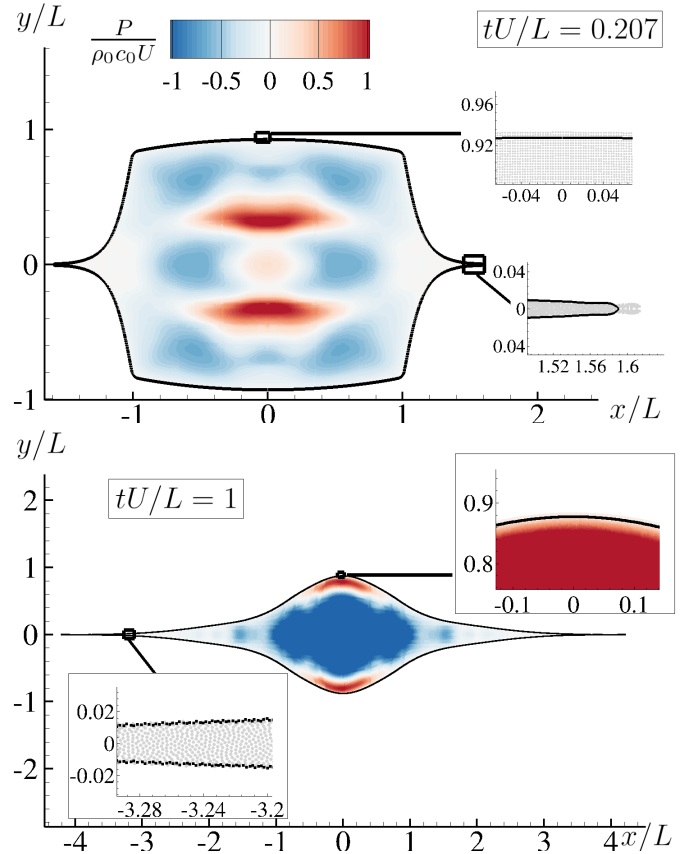

Fig. 14.   Impact of two identical inviscid fluid patches. Pressure field obtained with $L/\Delta x = 400$ at $tU/L = 0.207$ (top) and $tU/L = 1$ (bottom). In the top plot, the free-surface is compared to the one obtained in [12] with an incompressible Finite Volume method (LS-FVM); the LS-FVM time has been re-scaled for comparison purpose . In the bottom plot, the free-surface is compared with the one obtained using *QL-MassCons* scheme in [14].

impact velocity U. The error is less than 5×10^{-6} for all the resolution tested, and less than 2×10^{-7} for the finest resolution. Furthermore, while for the coarsest spatial resolution the error is oriented in the same direction, the finest resolution presents results oscillating around 0, without a preferential direction. Note that the horizontal component has also been checked, displaying a maximum error of $\dot{x}_G < 1 \times 10^{-6}U$.

V. Conclusion

In the present work, a globally non-conservative but locally accurate pressure gradient approximation has been adopted, resulting in a novel high-order weakly-compressible SPH scheme, which also prevents Tensile Instability occurrences. To fulfill the dynamic free-surface boundary condition, a switch between the non-conservative and conservative formulations has been used, the latter being retained in a thin region close to the free-surface. By contrast to the works in [9], [17] where similar non-conservative formulations were studied, recent advanced Particle Shifting Techniques have been adopted and introduced within the continuity and momentum equations through a quasi-Lagrangian formalism. The
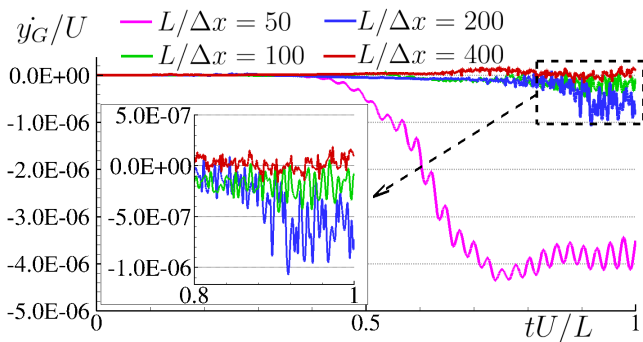
Fig. 15. Impact of two identical inviscid fluid patches. Temporal evolution of the vertical component of the velocity of the center of gravity y_G, normalized by the impact velocity U, for four spatial resolutions.

numerical diffusion has been introduced by means of Riemann solvers, filling another gap with [9], [17].

A numerical investigation has been carried out on several problems characterized by different flow features showing that, effectively, the proposed formulation allows for preventing drawbacks appearing with the conservative formulation of [14]. Particularly, whereas a saturation of the accuracy order was previously observed in [14] with conservative formulations, accuracy order between the first and third order has been noted with the proposed formulation, depending on the test case under investigation. Thanks to the non-occurrences of Tensile Instability, the fluid flow solution has also been shown less noisy than with conservative formulation in case of strong negative pressure. Since the proposed formulation does not intrinsically guarantee momenta conservation, the latter have been monitored proving that the overall errors are generally acceptable.

Future investigations shall focus on the relevance of solid boundary conditions, multi-phase flows and industrial application. Additionally, one can expect the present scheme may further benefit from the use of higher-order reconstructions such as the Weighted Essentially Non-Oscillatory (WENO) technique (see *e.g.* [2], [25], [26]).

REFERENCES

[1] M. Antuono, S. Marrone, A. Colagrossi, and B. Bouscasse. Energy balance in the δ-SPH scheme. *Computer Methods in Applied Mechanics and Engineering*, 289:209–226, 2015.

[2] D. Avesani, M. Dumbser, R. Vacondio, and M. Righetti. An alternative sph formulation: Ader-weno-sph. *Computer Methods in Applied Mechanics and Engineering*, 382:113871, 2021.

[3] S.S. Bishai Khanna. Standing waves of finite amplitude on surface of ideal liquid of finite depth. *Fluid Dynamics*, 13(2):187–191, 1978.

[4] A. Colagrossi, M. Antuono, and D. Le Touzé. Theoretical considerations on the free-surface role in the Smoothed-particle-hydrodynamics model. *Physical Review E*, 79(5):056701, 2009.

[5] A. Colagrossi, M. Antuono, A. Souto-Iglesias, and D. Le Touzé. Theoretical analysis and numerical verification of the consistency of viscous smoothed-particle-hydrodynamics formulations in simulating free-surface flows. *Physical Review E*, 84:026705, 2011.

[6] A. Colagrossi and M. Landrini. Numerical Simulation of Interfacial Flows by Smoothed Particle Hydrodynamics. *J. Comp. Phys.*, 191:448–475, 2003.

[7] G.A. Dilts. Moving-least-squares-particle hydrodynamics - I. Consistency and stability. *International Journal for Numerical Methods in Engineering*, 44(8):1115–1155, 1999.

[8] A. Khayyer, H. Gotoh, and Y. Shimizu. Comparative study on accuracy and conservation properties of two particle regularization schemes and proposal of an optimized particle shifting scheme in ISPH context. *Journal of Computational Physics*, 332:236–256, 2017.

[9] D. Le Touzé, A. Colagrossi, G. Colicchio, and M. Greco. A critical investigation of smoothed particle hydrodynamics applied to problems with free-surfaces. *International Journal for Numerical Methods in Fluids*, 73(7):660–691, 2013.

[10] S.J. Lind, P.K. Stansby, and B.D. Rogers. Incompressible–compressible flows with a transient discontinuous interface using smoothed particle hydrodynamics (SPH). *Journal of Computational Physics*, 309:129–147, 2016.

[11] S.J. Lind, R. Xu, P.K. Stansby, and B.D. Rogers. Incompressible smoothed particle hydrodynamics for free-surface flows: A generalised diffusion-based algorithm for stability and validations for impulsive flows and propagating waves. *Journal of Computational Physics*, 231(4):1499–1523, 2012.

[12] S. Marrone, A. Colagrossi, A. Di Mascio, and D. Le Touzé. Prediction of energy losses in water impacts using incompressible and weakly compressible models. *Journal of Fluids and Structures*, 54:802–822, 2015.

[13] S. Marrone, A. Colagrossi, D. Le Touzé, and G. Graziani. Fast free-surface detection and level-set function definition in SPH solvers. *Journal of Computational Physics*, 229(10):3652–3663, 2010.

[14] J. Michel, M. Antuono, G. Oger, and S. Marrone. Energy balance in quasi-Lagrangian Riemann-based SPH schemes. *Computer Methods in Applied Mechanics and Engineering*, 410:*, 2023.

[15] J. Michel, A. Vergnaud, G. Oger, C. Hermange, and D. Le Touzé. On Particle Shifting Techniques (PSTs): Analysis of existing laws and proposition of a convergent and multi-invariant law. *Journal of Computational Physics*, page 110999, 2022.

[16] J.J. Monaghan. Simulating Free Surface Flows with SPH. *Journal of Computational Physics*, 110(2):399–406, 1994.

[17] G. Oger, M. Doring, B. Alessandrini, and P. Ferrant. An improved SPH method: Towards higher order convergence. *Journal of Computational Physics*, 225(2):1472–1492, 2007.

[18] G. Oger, S. Marrone, D. Le Touzé, and M. De Leffe. SPH accuracy improvement through the combination of a quasi-Lagrangian shifting transport velocity and consistent ALE formalisms. *Journal of Computational Physics*, 313:76–98, 2016.

[19] A.N. Parshikov and S.A. Medin. Smoothed Particle Hydrodynamics using interparticle contact algorithms. *J. Comp. Phys.*, 180:358–382, 2002.

[20] N.J. Quinlan, M. Lastiwka, and M. Basa. Truncation error in meshfree particle methods. *International Journal for Numerical Methods in Engineering*, 66(13):2064–2085, 2006.

[21] P.W. Randles and L.D. Libersky. Smoothed Particle Hydrodynamics: some recent improvements and applications. *Computer methods in applied mechanics and engineering*, 39:375–408, 1996.

[22] P.N. Sun, A. Colagrossi, S. Marrone, M. Antuono, and AM. Zhang. A consistent approach to particle shifting in the δ-plus-sph model. *Computer Methods in Applied Mechanics and Engineering*, 348:912–934, 2019.

[23] P.N. Sun, A. Colagrossi, S. Marrone, and A.M. Zhang. The plus-SPH model: Simple procedures for a further improvement of the SPH scheme. *Computer Methods in Applied Mechanics and Engineering*, 315:25 – 49, 2017.

[24] W.G. Szymczak. Energy losses in non-classical free surface flows. In J.R. Blake, J.M. Boulton-Stone, and N.H. Thomas, editors, *Bubble Dynamics and Interface Phenomena*, volume 23 of *Fluid Mechanics and Its Applications*, pages 413–420. Springer Netherlands, 1994.

[25] A. Vergnaud, G. Oger, and D. Le Touzé. Investigations on a high order SPH scheme using WENO reconstruction. *Journal of Computational Physics*, page 111889, 2023.

[26] P.P. Wang, AM. Zhang, Z.F. Meng, F.R. Ming, and X.L. Fang. A new type of WENO scheme in SPH for compressible flows with discontinuities. *Computer Methods in Applied Mechanics and Engineering*, 381:113770, 2021.